

PHOTON SPLITTING CASCADES IN GAMMA-RAY PULSARS AND THE SPECTRUM OF PSR1509-58

Alice K. Harding, Matthew G. Baring¹

Laboratory for High Energy Astrophysics
NASA/Goddard Space Flight Center
Greenbelt, MD 20771

harding@twinkie.gsfc.nasa.gov, baring@lheavx.gsfc.nasa.gov

and

Peter L. Gonthier
Department of Physics
Hope College
Holland, MI 49423
gonthier@physics.hope.edu

ABSTRACT

Magnetic photon splitting $\gamma \rightarrow \gamma\gamma$, a QED process that becomes important only in magnetic fields approaching the quantum critical value, $B_{\text{cr}} = 4.41 \times 10^{13}$ Gauss, is investigated as a mechanism for attenuation of γ -rays emitted near the surface of strongly-magnetized pulsars. Since splitting has no threshold, it can attenuate photons and degrade their energies below the threshold for one-photon pair production, and in high enough fields it may dominate photon attenuation above pair threshold. We model photon splitting attenuation and subsequent splitting cascades in γ -ray pulsars, including the dipole field and curved spacetime geometry of the neutron star magnetosphere. We focus specifically on PSR1509-58, which has the highest surface magnetic field of all the γ -ray pulsars ($B_0 = 3 \times 10^{13}$ Gauss). We find that splitting will not be important for most γ -ray pulsars, i.e. those with $B_0 \lesssim 0.2B_{\text{cr}}$, either in competition with pair production attenuation in pair cascades, or in photon escape cutoffs in the spectrum. Photon splitting *will* be important for γ -ray pulsars having $B_0 \gtrsim 0.3B_{\text{cr}}$, where the splitting attenuation lengths and escape energies become comparable to or less than those for pair production. We compute Monte Carlo spectral models for PSR1509-58, assuming that either a full photon splitting cascade or a combination of splitting and pair production (depending on which splitting modes operate) attenuate a power-law input spectrum. We find that photon splitting, or combined splitting and pair production, can explain the unusually low cutoff energy (between 2 and 30 MeV) of PSR1509-58,

¹Compton Fellow, Universities Space Research Association

and that the model cascade spectra, which display strong polarization, are consistent with the observed spectral points and upper limits for polar cap emission at a range of magnetic colatitudes up to $\sim 25^\circ$.

Subject headings: gamma rays: pulsars: theory - pulsars: individual: (PSR1509-58)

1. INTRODUCTION

The discovery of at least five new γ -ray pulsars by the Compton Gamma-Ray Observatory (CGRO) and ROSAT has re-ignited theoretical work on the physical processes and modeling of high-energy radiation from pulsars. Including the previously known γ -ray pulsars, Crab (Nolan et al. 1993) and Vela (Kanbach et al. 1994), the recent detection of pulsed γ -rays from PSR B1706-44 (Thompson et al. 1992), Geminga (Halpern & Holt 1992, Bertsch et al. 1992), PSR1509-58 (Wilson et al. 1993), PSR B1055-52 (Fierro et al. 1993), PSR B1951+32 (Ramanamurthy et al. 1995) and possibly PSR0656+14 (Ramanamurthy et al. 1996) bring the total to at least seven. For the first time, it is possible to look for the similarities and patterns in the γ -ray emission characteristics that may reveal clues to the origin of this emission. Examples are a preponderance of double pulses, a γ -ray luminosity vs. polar cap current correlation, a spectral hardness vs. characteristic age correlation, and spectral cutoffs above a few GeV (e.g. Thompson 1996). PSR1509-58 stands out among the known γ -ray pulsars as having both an unusually low spectral cutoff energy (somewhere between 2 and 30 MeV) and the highest inferred surface magnetic field (3×10^{13} Gauss). It has been detected by the CGRO instruments operating only in the lowest energy bands, BATSE (Wilson et al. 1993) and OSSE (Matz et al. 1994), with the higher energy instruments, COMPTEL (Bennett et al. 1993) and EGRET (Nel et al. 1996), giving upper limits that require a cutoff or turnover between 2 and 30 MeV. There is no evidence for pulsed TeV emission (Nel et al. 1992).

There are currently two types of models for γ -ray pulsars being investigated in detail. Polar cap models assume that particles are accelerated along open field lines near the neutron star by strong parallel electric fields (e.g. Arons 1983). The primary particles induce electromagnetic cascades through the creation of electron-positron pairs by either curvature radiation (Daugherty & Harding 1982, 1994, 1996) or inverse-Compton radiation (Sturner & Dermer 1994) γ -rays. Outer gap models assume that the primary particles are accelerated along open field lines in the outer magnetosphere, near the null charge surface, where the corotation charge changes sign, and where strong electric fields may develop (Cheng, Ho & Ruderman 1986a,b; Chiang & Romani 1992; Romani & Yadigaroglu 1995). Since the magnetic fields in the outer gaps are too low to sustain one-photon pair production cascades, these models must rely on photon-photon pair production of γ -rays, interacting with either non-thermal X-rays from the gap or thermal X-rays from the neutron star surface, to initiate pair cascades.

Magnetic one-photon pair production, $\gamma \rightarrow e^+e^-$, has so far been the only photon attenuation mechanism assumed to operate in polar cap cascade models. Another attenuation mechanism,

photon splitting $\gamma \rightarrow \gamma\gamma$, will also operate in the high-field regions near pulsar polar caps but has not yet been included in polar cap model calculations. The rate of photon splitting increases rapidly with increasing field strength (Adler 1971), so that it may even be the dominant attenuation process in the highest field pulsars. There are several potentially important consequences of photon splitting for γ -ray pulsar models. Since photon splitting has no threshold, it can attenuate photons below the threshold for pair production, $\varepsilon = 2/\sin \theta_{kB}$, and can thus produce cutoffs in the spectrum at lower energies. Here θ_{kB} is the angle between the photon momentum and the magnetic field vectors, and ε is (hereafter) expressed in units of $m_e c^2$. When the splitting rate becomes large enough, splitting can take place during a photon's propagation through the neutron star magnetosphere *before* the pair production threshold is crossed (i.e. before an angle $\sim 2/\varepsilon$ to the field is achieved). Consequently, the production of secondary electrons and positrons in pair cascades will be suppressed. Instead of *pair* cascades, one could have *splitting* cascades, where the high-energy photons split repeatedly until they escape the magnetosphere. The potential importance of photon splitting in neutron star applications was suggested by Adler (1971), Mitrofanov *et al.* (1986) and Baring (1988). Its attenuation and reprocessing properties have been explored in the contexts of annihilation line suppression in gamma-ray pulsars (Baring 1993), and spectral formation of gamma-ray bursts from neutron stars (Baring 1991). Photon splitting cascades have also been investigated in models of soft γ -ray repeaters, where they will soften the photon spectrum very efficiently with no production of pairs (Baring 1995, Baring & Harding 1995a, Harding & Baring 1996, Chang *et al.* 1996).

In this paper we examine the importance of photon splitting in γ -ray pulsar polar cap models (it presumably will not operate in the low fields of outer gap models). Following a brief discussion of the physics of photon splitting in Section 2, we present calculations of the splitting attenuation lengths and escape energies in the dipole magnetic field of a neutron star. A preliminary study (Harding, Baring & Gonthier 1996) has shown that splitting will be the primary mode of attenuation of γ -rays emitted parallel to a magnetic field $B \gtrsim 0.3B_{cr} = 1.3 \times 10^{13}$ Gauss. We then present, in Section 3, photon splitting cascade models for two cases: (1) when only one mode of splitting ($\perp \rightarrow \parallel \parallel$) allowed by the kinematic selection rules (Adler 1971, Shabad 1975) operates, suppressing splitting of photons of parallel polarization (so that they can only pair produce), but still permitting photons of perpendicular polarization to either split once or produce pairs, and (2) when the three splitting modes allowed by CP (charge-parity) invariance operate, producing mode switching and a predominantly photon splitting cascade. In Section 4, model cascade spectra are compared to the observed spectrum of PSR1509-58 to determine the range of magnetic colatitude emission points (if any) that can produce a spectral cutoff consistent with the data. These spectra have cutoff energies that are decreasing functions of the magnetic colatitude. It is found that a reasonably broad range of polar cap sizes will accommodate the data, and that strong polarization signatures appear in the spectra due to the action of photon splitting.

2. PHOTON SPLITTING AND PAIR CREATION ATTENUATION

The basic features of magnetic photon splitting $\gamma \rightarrow \gamma\gamma$ and the more familiar process of single-photon pair creation $\gamma \rightarrow e^+e^-$ are outlined in the next two subsections before investigating their role as photon attenuation mechanisms in pulsar magnetospheres. Note that throughout this paper, energies will be rendered dimensionless, for simplicity, using the scaling factor $m_e c^2$. Magnetic fields will also often be scaled by the critical field B_{cr} ; this quantity will be denoted by a prime: $B' = B/B_{\text{cr}}$.

2.1. Photon Splitting Rates

The splitting of photons in two in the presence of a strong magnetic field is an exotic and comparatively recent prediction of quantum electrodynamics (QED), with the first correct calculations of the reaction rate being performed in the early '70s (Bialynicka-Birula and Bialynicki-Birula 1970; Adler *et al.* 1970; Adler 1971). Its relative obscurity to date (compared, for example, with magnetic pair creation) in the astrophysical community stems partly from the mathematical complexity inherent in the computation of the rate. Splitting is a third-order QED process with a triangular Feynman diagram. Hence, though splitting is kinematically possible, when $B = 0$ it is forbidden by a charge conjugation symmetry of QED known as Furry's theorem (e.g. see Jauch and Rohrlich, 1980), which states that ring diagrams that have an odd number of vertices with only external photon lines generate interaction matrix elements that are identically zero. This symmetry is broken by the presence of an external field. The splitting of photons is therefore a purely quantum effect, and has appreciable reaction rates only when the magnetic field is at least a significant fraction of the quantum critical field $B_{\text{cr}} = m_e^2 c^3 / (e\hbar) = 4.413 \times 10^{13}$ Gauss. Splitting into more than two photons is prohibited in the limit of zero dispersion because of the lack of available quantum phase space (Minguzzi 1961).

The reaction rate for splitting is immensely complicated by dispersive effects (e.g. Adler 1971; Stoneham 1979) caused by the deviation of the refractive index from unity in the strong field. Consequently, manageable expressions for the rate of splitting are only possible in the limit of zero dispersion, and are still then complicated triple integrations (see Stoneham 1979, and also Bařer, Mil'shtein, and Shaĭsultanov 1986 for electric field splitting) due to the presence of magnetic electron propagators in the matrix element. Hence simple expressions for the rate of splitting of a photon of energy ω in a field B were first obtained by Bialynicka-Birula and Bialynicki-Birula (1970), Adler *et al.* (1970) and Adler (1971) in the low-energy, non-dispersive limit: $\omega B/B_{\text{cr}} \lesssim 1$. The total rate in this limit, averaged over photon polarizations (Papanyan and Ritus, 1972), is expressible in terms of an attenuation coefficient

$$T_{\text{sp}}(\omega) \approx \frac{\alpha^3}{10\pi^2} \frac{1}{\lambda} \left(\frac{19}{315} \right)^2 B'^6 \mathcal{C}(B') \omega^5 \sin^6 \theta_{\text{kB}} \quad , \quad (1)$$

where $\alpha = e^2/\hbar c \approx 1/137$ is the fine structure constant, $\lambda = \hbar/(m_e c)$ is the Compton wavelength

of the electron, and θ_{kB} is the angle between the photon momentum and the magnetic field vectors. Here $\mathcal{C}(B')$ is a strong-field modification factor (derivable, for example, from Eq. 41 of Stoneham, 1979: see Eq. [5] below) that approximates unity when $B \ll B_{cr}$ and scales as B^{-6} for $B \gg B_{cr}$.

The corresponding differential spectral rate for the splitting of photons of energy ω (with $\omega \ll 1$) into photons of energies ω' and $\omega - \omega'$ is

$$T_{sp}(\omega, \omega') \approx 30 \frac{\omega'^2(\omega - \omega')^2}{\omega^5} T_{sp}(\omega) . \quad (2)$$

Equations (1) and (2) are valid (Baring, 1991) when $\omega B' \sin \theta_{kB} \lesssim 1$, which for pulsar fields and $\omega \sin \theta_{kB} \lesssim 2$, generally corresponds to the regime of weak vacuum dispersion. Reducing θ_{kB} or B dramatically increases the photon energy required for splitting to operate in a neutron star environment. The produced photons emerge at an angle θ_{kB} to the field since splitting is a collinear process in the low-dispersion limit.

Adler (1971) observed that in the low-energy limit, the splitting rate was strongly dependent on the polarization states of the initial and final photons; this feature prompted the suggestion by Adler et al. (1970) and Usov and Shabad (1983) that photon splitting should be a powerful polarizing mechanism in pulsars. The polarization-dependent rates can be taken from Eq. (23) of Adler (1971), which can be related to equations (1) or (2) via

$$T_{\perp \rightarrow \parallel \parallel}^{sp} = \frac{1}{2} T_{\parallel \rightarrow \perp \parallel}^{sp} = \left(\frac{\mathcal{M}_1^2}{\mathcal{M}_2^2} \right)^2 T_{\perp \rightarrow \perp \perp}^{sp} = \frac{2\mathcal{M}_1^2 T_{sp}}{3\mathcal{M}_1^2 + \mathcal{M}_2^2} , \quad (3)$$

where the scattering amplitude coefficients

$$\begin{aligned} \mathcal{M}_1 &= \frac{1}{B'^4} \int_0^\infty \frac{ds}{s} e^{-s/B'} \left\{ \left(-\frac{3}{4s} + \frac{s}{6} \right) \frac{\cosh s}{\sinh s} + \frac{3 + 2s^2}{12 \sinh^2 s} + \frac{s \cosh s}{2 \sinh^3 s} \right\} \\ \mathcal{M}_2 &= \frac{1}{B'^4} \int_0^\infty \frac{ds}{s} e^{-s/B'} \left\{ \frac{3}{4s} \frac{\cosh s}{\sinh s} + \frac{3 - 4s^2}{4 \sinh^2 s} - \frac{3s^2}{2 \sinh^4 s} \right\} \end{aligned} \quad (4)$$

are given in Adler (1971) and Eq. 41 of Stoneham (1979). In the limit of $B \ll B_{cr}$, $\mathcal{M}_1 \approx 26/315$ and $\mathcal{M}_2 \approx 48/315$, while in the limit of $B \gg B_{cr}$, equation (4) produces $\mathcal{M}_1 \approx 1/(6B'^3)$ and $\mathcal{M}_2 \approx 1/(3B'^4)$. The factor of two in the numerator of the right hand side of equation (3) accounts for the duplicity of photons produced in splitting. The photon polarization labelling convention of Stoneham (1979) is adopted here (this standard form was not used by Adler, 1971): the label \parallel refers to the state with the photon's *electric* field vector parallel to the plane containing the magnetic field and the photon's momentum vector, while \perp denotes the photon's electric field vector being normal to this plane. Summing over the polarization modes yields the relationship for the strong-field modification factor in equation (1):

$$\mathcal{C}(B') = \frac{1}{12} \left(\frac{315}{19} \right)^2 (3\mathcal{M}_1^2 + \mathcal{M}_2^2) . \quad (5)$$

Note that, in the absence of vacuum dispersion, the splitting modes $\perp\rightarrow\perp\parallel$, $\parallel\rightarrow\perp\perp$ and $\parallel\rightarrow\parallel\parallel$ are forbidden by arguments of CP (charge-parity) invariance in QED (Adler 1971); dispersive effects admit the possibility of non-collinear photon splitting so that there is a small but non-zero probability for the $\perp\rightarrow\perp\parallel$ channel. Equations (1)–(5) define the rates to be used in the analyses of this paper, and are valid for $\omega B' \sin \theta_{kB} \ll 1$. The triple integral expressions that Stoneham (1979) derives are valid (below pair creation threshold) for a complete range (i.e. 0 to ∞) of the expansion parameter $\omega B' \sin \theta_{kB}$, but are not presently in a computational form suitable for use here. Work is in progress to address this deficiency (Baring & Harding 1996), and preliminary results indicate that equations (1)–(5) approximate Stoneham’s (1979) formulae to better than two percent for $\omega B' \sin \theta_{kB} \leq 0.2$, and differs by at most a factor of around 2.5 for $\omega B' \sin \theta_{kB} \sim 1.5$, the value relevant to the calculations of this paper; the splitting rate given by Stoneham’s formulae initially increase above the low energy limits as $\omega B' \sin \theta_{kB}$ increases.

Recently there has appeared a new result on the rates of photon splitting. Mentzel, Berg & Wunner (1994) presented an S-matrix calculation of the rates for the three polarization modes permitted by CP invariance that are considered here. While their formal development is comparable to an earlier S-matrix formulation of splitting in Melrose & Parle (1983a,b), their presentation of numerical results appeared to be in violent disagreement (see also their astrophysical presentation in Wunner, Sang & Berg 1995) with the splitting results obtained via the Schwinger proper-time technique by Adler (1971) and Stoneham (1979) that comprise equations (1)–(5) here. These results have now been retracted, the disagreement being due to a sign error in their numerical code (Wilke & Wunner 1996). The revised results are in much better agreement with the rates computed by Adler (1971). However, the revised numerical splitting rates of Wilke & Wunner (1996) still differ by as much as a factor of 3 from Baring & Harding’s (1996) computations of Stoneham’s (1979) general formulae. Bȧer, Mil’shtein, & Shȧsultanov (1996) generate numerical results from their earlier alternative proper-time calculation (Bȧer, Mil’shtein, & Shȧsultanov 1986) that are in accord with Stoneham’s and Adler’s (1971) results and also with those of Baring & Harding (1996). The numerical computation of the S-matrix formalism is a formidable task. The proper-time analysis, though difficult, is more amenable, and has been reproduced in the limit of $B \ll B_{cr}$ by numerous authors. As the S-matrix and proper-time techniques should produce equivalent results, and indeed have done so demonstrably in the case of pair production (see DH83 and Tsai & Erber 1974), we choose to use the amenable proper-time results outlined above in the calculations of this paper.

The above results ignore the fact that the magnetized vacuum is dispersive and birefringent, so that the phase velocity of light is less than c and depends on the photon polarization. Dispersion can therefore alter the kinematics of QED processes such as splitting (Adler 1971), and further dramatically complicates the formalism for the rates (Stoneham 1979). Extensive discussions of dispersion in a magnetized vacuum are presented by Adler (1971) and Shabad (1975); considerations of plasma dispersion are not relevant to the problem of gamma-ray emission from pulsars because they become significant only for densities in excess of around 10^{27} cm^{-3} , which are only attained

at the stellar surface. Adler (1971) showed that in the limit of *weak* vacuum dispersion (roughly delineated by $B' \sin \theta_{kB} \lesssim 1$), where the refractive indices for the polarization states are *very* close to unity, energy and momentum could be simultaneously conserved only for the splitting mode $\perp \rightarrow \parallel\parallel$ (of the modes permitted by CP invariance) below pair production threshold. This kinematic selection rule was demonstrated for subcritical fields, where the dispersion is very weak, a regime that generally applies to gamma-ray pulsar scenarios. Therefore, it is probable that only the one mode ($\perp \rightarrow \parallel\parallel$) of splitting operates in gamma-ray pulsars. This result may be modified by subtle effects such as those incurred by field non-uniformity. We adopt a dual scenario in this paper for the sake of completeness: one in which all CP-permitted modes of splitting operate, and one in which Adler’s kinematic selection rules are imposed. Note that in magnetar models of soft gamma repeaters (e.g Baring 1995, Harding and Baring 1996), where supercritical fields are employed, moderate vacuum dispersion arises. In such a regime, it is not clear whether Adler’s selection rules still endure, since his analysis implicitly uses weak dispersion limits of linear vacuum polarization results (e.g. see Shabad 1975), and omits higher order contributions (e.g. see Melrose and Parle 1983a,b) to the vacuum polarization (for example, those that couple to photon absorption via splitting) that become prominent in supercritical fields. Furthermore, plasma dispersion effects may be quite pertinent to soft gamma repeater models (e.g. Bulik and Miller 1996), rendering them distinctly different from pulsar scenarios.

2.2. Pair Production Rate

One-photon pair production is a first-order QED process that is quite familiar to pulsar theorists. It is forbidden in field-free regions due to the imposition of four-momentum conservation, but takes place in an external magnetic field, which can absorb momentum perpendicular to \mathbf{B} . The rate (Toll 1952, Klepikov 1954) increases rapidly with increasing photon energy and transverse magnetic field strength, becoming significant for γ -rays above the threshold, $\omega = 2/\sin \theta_{kB}$, and for fields approaching B_{cr} . When the photon energy is near threshold, there may be only a few kinematically available pair states, and the rate will be resonant at each pair state threshold, producing a sawtooth structure (Daugherty & Harding 1983, hereafter DH83). For photon energies well above threshold, the number of pair states becomes large, allowing the use of a more convenient asymptotic expression for the polarization dependent attenuation coefficient (Klepikov 1954, Tsai & Erber 1974):

$$T_{\parallel,\perp}^{pp} = \frac{1}{2} \frac{\alpha}{\lambda} B' \sin \theta_{kB} \Lambda_{\parallel,\perp}(\chi), \quad (6)$$

$$\Lambda_{\parallel,\perp}(\chi) \approx \begin{cases} (0.31, 0.15) \exp\left(-\frac{4}{3\chi}\right) & \chi \ll 1 \\ (0.72, 0.48) \chi^{-1/3} & \chi \gg 1 \end{cases} \quad (7)$$

where $\chi \equiv (\omega/2)B' \sin \theta_{kB}$.

In polar cap pulsar models (e.g. Sturrock 1971, Ruderman and Sutherland 1975), high energy radiation is usually emitted at very small angles to the magnetic field, well below pair threshold (see Harding 1995, for review). The γ -ray photons will convert into pairs only after they have traveled a distance s comparable to the field line radius of curvature ρ , so that $\sin \theta_{kB} \sim s/\rho$. From the above expression, the pair production rate will be vanishingly small until the argument of the exponential approaches unity, i.e. when $\omega B' \sin \theta_{kB} \gtrsim 0.2$. Consequently, pair production will occur well above threshold when $B \ll 0.1B_{cr}$ and the asymptotic expression will be valid. However when $B \gtrsim 0.1B_{cr}$, pair production will occur at or near threshold, where the asymptotic expression has been shown to fall orders of magnitude below the exact rate (DH83). In the present calculation, we approximate the near-threshold reduction in the asymptotic pair production attenuation coefficient by making the substitution, $\chi \rightarrow \chi/F$, where $F = 1 + 0.42(\omega \sin \theta_{kB}/2)^{-2.7}$ in equation (7) (DH83). Baring (1988) has derived an analytic expression for the one-photon pair production rate near threshold which gives a result that agrees numerically with the approximation of DH83.

Yet even the near-threshold correction to the asymptotic rate becomes poor when $B \gg 0.1B_{cr}$ and the photons with parallel and perpendicular polarization produce pairs only (DH83) in the ground (0,0) and first excited (0,1) and (1,0) states respectively. Here (j, k) denotes the Landau level quantum numbers of the produced pairs. Therefore when the local $B > 0.1B_{cr}$, instead of the asymptotic form in equation (7), we use the exact, polarization-dependent, pair production attenuation coefficient (DH83), including only the (0,0) pair state for \parallel polarization:

$$T_{\parallel}^{pp} = \frac{\alpha \sin \theta_{kB}}{\lambda \xi |p_{00}|} \exp(-\xi), \quad \omega \geq 2/\sin \theta_{kB} \quad , \quad (8)$$

and only the sum of the (0,1) and (1,0) states for \perp polarization:

$$T_{\perp}^{pp} = \frac{\alpha \sin \theta_{kB}}{\lambda \xi |p_{01}|} (E_0 E_1 + 1 + p_{01}^2) \exp(-\xi), \quad \omega \geq \frac{1 + (1 + 2B')^{1/2}}{\sin \theta_{kB}} \quad (9)$$

where

$$E_0 = (1 + p_{01}^2)^{1/2} \quad , \quad E_1 = (1 + p_{01}^2 + 2B')^{1/2}$$

for

$$|p_{jk}| = \left[\frac{\omega^2}{4} \sin^2 \theta_{kB} - 1 - (j+k)B' + \left(\frac{(j-k)B'}{\omega \sin \theta_{kB}} \right)^2 \right]^{1/2}$$

and

$$\xi = \frac{\omega^2}{2B'} \sin^2 \theta_{kB} \quad . \quad (10)$$

Actually, both the asymptotic and exact mean-free paths ($1/T_{pp}$) are so small in fields where photons pair produce at threshold that it is, in fact, not important which rate is used at very high field strengths (i.e. $B' \gtrsim 1$). The pair production rate in this regime thus behaves like a wall at threshold and photons will pair produce as soon as they satisfy the kinematic restrictions on ω given in equations (8) and (9). The creation of bound pairs rather than free pairs is possible in fields $B' \gtrsim 0.1$ (Usov & Melrose 1995), but this should not affect the present calculation since we do not model the full pair cascade.

2.3. Attenuation Lengths

To assess the relative importance of photon splitting compared to pair production through a dipole magnetic field, we compute the attenuation length L , defined to be the path length over which the optical depth is unity:

$$\tau(\theta, \varepsilon) = \int_0^L T(\theta_{kB}, \omega) ds = 1 \quad , \quad (11)$$

where ds is the pathlength differential along the photon momentum vector \mathbf{k} and T is the attenuation coefficient for either splitting, T_{sp} , or pair production, T_{pp} . In this paper, attenuation lengths are computed as averages over polarizations of the initial photon and, for splitting, sums over the final polarization states. Here θ_{kB} and the photon energy $k^\theta = \omega$ are functions of the position (e.g. see equation [A1]), specifically measured in the local inertial frame, while θ is the colatitude of emission and ε is the photon energy to an observer at infinity; our treatment of curved spacetime is discussed immediately below. In regions where the path length is much shorter than both the scale length of the field strength variation or the radius of curvature of the field, L reduces to the inverse of the attenuation coefficient. In the calculation of the splitting attenuation lengths, all three CP-permitted modes are assumed to operate. The attenuation length behavior of the individual modes are similar.

We assume that test photons are emitted at the neutron star surface and propagate outward, initially parallel or at a specified angle, $\theta_{kB,0}$ to the dipole magnetic field (see Fig. 1 for a depiction of the geometry). Photon emission in polar cap models of gamma-ray pulsars can occur above the stellar surface (but see the discussion in Section 5), which would generate attenuation lengths somewhat longer than those determined here, due to the r^{-3} decay of the field. A surface origin of the photons is chosen in this paper to provide a simple and concise presentation of the attenuation properties. We have included the general relativistic effects of curved spacetime in a Schwarzschild metric, following the treatment of Gonthier & Harding (1994, GH94) who studied the effects of general relativity on photon attenuation via magnetic pair production. GH94 included the curved spacetime photon trajectories, the magnetic dipole field in a Schwarzschild metric and the gravitational redshift of the photon energy. One improvement we have made here to the treatment of GH94 is to explicitly keep track of the gravitational redshift of the photon energy as a function of distance from the neutron star (see Appendix for details). Our analysis is confined to the Schwarzschild metric because the dynamical timescales for gamma-ray pulsars are considerably shorter than their period (e.g. $P = 0.15$ sec. for PSR1509-58), so that rotation effects in the Kerr metric can be neglected. We have taken a neutron star mass, $M = 1.4 M_\odot$ and radius, $R = 10^6$ cm in these calculations.

Fig. 2 illustrates how the attenuation lengths for photon splitting and pair production vary with energy for different magnetic colatitudes of the emission point, for surface fields of $B_0 = 0.1B_{cr}$, and $B_0 = 0.7B_{cr}$. A field of $B_0 = 0.7B_{cr}$ is the value of the polar surface field derived from the magnetic dipole spin-down energy loss (Shapiro & Teukolsky 1983), using the measured P and

\dot{P} for PSR1509-58. As noted by Usov & Melrose (1995), this is exactly twice the value of the surface field given by formulae in other sources (Manchester & Taylor 1977, Michel 1991), which assume (inaccurately) that the dipole magnetic moment $\mu = B_0 R^3$ rather than $\mu = B_0 R^3/2$ for a uniformly magnetized sphere of radius R . The other γ -ray pulsars have surface field strengths in the range $1 - 9 \times 10^{12}$ G, or $0.02 - 0.2 B_{\text{cr}}$ (the Crab and Vela pulsars have fields around $0.2 B_{\text{cr}}$). Note that the attenuation lengths in Fig. 2 are for unpolarized radiation; the curves for \parallel and \perp polarization states look very similar.

The curves in Fig. 2 have a power-law behavior at high energies, i.e. for attenuation lengths much less than 10^6 cm, where the dipole field is almost uniform in direction and of roughly constant strength. They also exhibit sharp increases at the low energy end, where photons begin to escape the magnetosphere without attenuation. We may estimate the behavior of the power-law portions of the attenuation length curves in Fig 2 as follows. Since the photons are assumed to initially propagate parallel to the field, the field curvature will give propagation oblique to the field only after significant distances are traversed, so that the obliquity of the photon to the field scales, to first order, as the distance travelled, $\sin \theta_{\text{KB}} \propto s$. Inserting this in equation (1) gives a photon splitting attenuation coefficient $\propto s^6$ i.e. an optical depth $\propto \varepsilon^5 s^7$, since $T_{\text{sp}} \propto \varepsilon^5$. Inversion then indicates that the attenuation length should vary as $L \propto \varepsilon^{-5/7}$: this is borne out in Fig. 2. For $B_0 \gtrsim 0.1 B_{\text{cr}}$, pair production occurs as soon as the threshold $\varepsilon_{\text{th}} = 2/\sin \theta_{\text{KB}}$ is crossed (cf. Section 2.2) during the photon propagation in the magnetosphere. Essentially, due to the enormous creation rate immediately above the threshold, this energy serves as an impenetrable “wall” to the photon. Again, since $\sin \theta_{\text{KB}} \propto s$ in the early stages of propagation, the pair production attenuation length should scale as $L \propto 2/\varepsilon$. These proportionalities hold in both curved and flat spacetime since general relativistic effects distort spacetime in a smooth and differentiable manner (see the Appendix). However, the attenuation lengths computed in the Schwarzschild metric are about a factor of 1.5 lower than those computed in flat spacetime (Baring & Harding 1995b).

The photon splitting attenuation coefficient we have used is strictly valid only below pair threshold. Hence, the attenuation lengths for splitting depicted in Fig. 2 can be regarded as only being symbolic when they exceed those for pair production, since then pair threshold is reached before splitting occurs. No technically amenable general expressions for the rate of splitting above pair threshold exist in the physics literature. But the vicinity of parameter space just below pair threshold is the regime of importance for γ -ray pulsar models, where the emitted photons propagate until they either split or they reach pair threshold, in which case they pair produce. The attenuation length curves near the crossover points in Fig. 2 for $B_0 = 0.7 B_{\text{cr}}$ will require inclusion of high energy corrections to the attenuation coefficient (Stoneham 1979) that arise as the $\gamma \rightarrow e^+ e^-$ threshold is approached. Currently work is in progress to compute these modifications (Baring and Harding 1996, in preparation), and preliminary results indicate that the rate in equation (1) is quite accurate for $B \lesssim 0.2 B_{\text{cr}}$, but increases by factors of at most a few for $B = 0.7 B_{\text{cr}}$ and $\omega = 2$, as mentioned in Section 2.1 above.

2.4. Escape Energies

The energy at which the attenuation length becomes infinite defines the *escape energy*, below which the optical depth is always $\ll 1$, and photons escape the magnetosphere; the existence of such an escape energy is a consequence of the r^{-3} decay of the dipole field. Escape energies of unpolarized photons for both photon splitting and pair production are shown in Fig. 3 as a function of magnetic colatitude θ of the photon emission point for different values of magnetic field strength (see also Harding, Baring and Gonthier, 1996). The escape energies clearly decline with θ and are monotonically decreasing functions of B for the range of fields shown. The divergences as $\theta \rightarrow 0$ are due to the divergence of the field line radius of curvature at the poles. There the maximum angle θ_{kB} achieved before the field falls off and inhibits attenuation is proportional to the colatitude θ . For photon splitting, since the rate in equation (1) is proportional to $\omega^5 \sin^6 \theta_{kB}$, and therefore also the attenuation length L , it follows that the escape energy scales as $\varepsilon_{esc} \propto \theta^{-6/5}$ near the poles (see also Fig. 5) as is determined by the condition $L \sim R$. For pair production, the behaviour of the rate (and therefore L) is dominated by the exponential form in equation (7), which then quickly yields a dependence $\varepsilon_{esc} \propto \theta^{-1}$ near the poles for $B_0 \lesssim 0.1 B_{cr}$. This behaviour extends to higher surface fields because production then is at threshold, which determines $\varepsilon_{esc} \sim 2/\theta_{kB} \propto \theta^{-1}$. At high fields, $B_0 \gtrsim 0.3 B_{cr}$, there is a saturation of the photon splitting attenuation lengths and escape energies, due to the diminishing dependence of B in the attenuation coefficient. Likewise, there is a saturation of the pair production escape energy at fields above which pair production occurs at threshold. The pair production escape energy curves are bounded below by the pair threshold $2/\sin \theta_{kB}$ and merge for high θ , at the pair rest mass limit, $\varepsilon = 2$, blueshifted by the factor $(1 - 2GM/Rc^2)^{-1/2} \sim 1.3$. Note that photon splitting can attenuate photons well below pair threshold. For low fields, pair production escape energies are below those for splitting, but in high fields, splitting escape energies are lower at all θ . The escape energies are roughly equal for $B_0 \sim 0.3 B_{cr}$.

The effects of curved spacetime are quite significant when compared to the attenuation lengths and the escape energies obtained assuming flat spacetime. A comparison of the escape energies for splitting and pair production, computed in flat and curved spacetime, is shown in Fig. 4. The largest effects are due to the increase of the surface dipole field strength by roughly a factor of 1.4, and the correction for the gravitational redshift of the photon, which increases the photon energy by roughly a factor 1.2 in the local inertial frame at the neutron star surface compared to the energy measured by the observer in flat space (see the Appendix). The combination of these effects decreases the photon splitting escape energy by a factor of about 2 compared to flat spacetime. The decrease in escape energy for pair production is also a factor of about 2, except at the largest values of θ and B' , where the pair rest mass limit is reached (cf. Fig. 3) The escape energy is then no longer dependent on field strength, and the ratio of the curved to flat space escape energy is just the redshift of the photon energy (~ 0.8) from the conversion point. This is achieved in the upper right hand corner of the figure; photon splitting has no such strict limit. The ratios also become insensitive to θ near the poles since there the photons move almost radially, thus traveling

along straight trajectories, and the curved-space correction to the field is not changing rapidly with colatitude. The curvature of the photon trajectory in a Schwarzschild metric does not affect the escape energies, to first order, except in the case of emission at large colatitudes, where the photon wavevector makes a large angle to the radial direction.

High energy emission from curvature radiation, inverse Compton or synchrotron by relativistic particles with Lorentz factor Γ will not beam the photons precisely along the magnetic field, but within some angle $\sim 1/\Gamma$ to the field. Fig. 5 illustrates the effect on the escape energies of a non-zero angle of emission of the photons, for the case where the photons are emitted at angles toward the dipole axis. We have chosen the angle $\theta_{kB,0} = .01$ rad ($= 0.57^\circ$) because it would be the angle at which photons with $\epsilon \sim 100$ would be emitted through the cyclotron upscattering process, $\theta_{kB,0} \simeq B'/\epsilon$ (Dermer 1990). For emission angles $\theta_{kB,0} = 0$ in Fig. 5a, which plots ε_{esc} for photon splitting, $\varepsilon_{esc} \propto B_0^{-6/5}$ for $B_0 \lesssim 0.3B_{cr}$ and $\varepsilon_{esc} \propto \theta^{-6/5}$, for $\theta \lesssim 20^\circ$, dependences that naturally follow from the form of equation (1). Generally, the escape energy is insensitive to the emission angle for $\theta \gtrsim 10\theta_{kB,0}$. For small angles, the escape energy decreases and the $\theta_{kB,0} = .57^\circ$ curves flatten below the $\theta_{kB,0} = 0$ curves, converging as $\theta \rightarrow 0$ to an energy that is proportional to $(B_0 \sin \theta_{kB,0})^{-6/5}$ (see Eq. [15]). This convergence is a consequence of the field along photon trajectories that originate near the pole being almost uniform and tilted at about angle $\theta_{kB,0}$ to the photon path. In Fig. 5b, the same effect is seen for pair creation, but this time the “saturation” is at the redshifted threshold energy $2(1 - 2GM/Rc^2)^{1/2}/\sin \theta_{kB,0}$, and is independent of B_0 . We note that this behaviour at low colatitudes was observed, in the case of pair creation in flat spacetime, by Chang, Chen and Ho (1996).

An obvious exception to this expected behaviour is seen in Fig. 5b for the $B' = 3.1$ curve, where the escape energy is actually *larger* at small colatitudes ($1^\circ \lesssim \theta \lesssim 10^\circ$) when the emission angle $\theta_{kB,0}$ is increased. This counter-intuitive result can be understood with the aid of Fig. 6, which shows the increase in $\sin \theta_{kB}$, and $\omega \sin \theta_{kB}$, determined in the local inertial frame, with path length s along the photon trajectory. Note that (i) the $\theta_{kB,0} = 0$ curves increase in proportion to s when $s/R \ll 1$, as described in the Appendix, and (ii) the $\sin \theta_{kB}$ curves increase logarithmically with s/R when s/R is not very small. In this large field, pair production occurs when the threshold $\omega \sin \theta_{kB} = 2$ is crossed, at the same path length for both $\theta_{kB,0} = 0$ and $\theta_{kB,0} = 0.57^\circ$. The differences in the photon trajectories (which are almost radial) for these two cases are so small that s effectively represents the same height above the stellar surface for both $\theta_{kB,0}$. Since $\omega \sin \theta_{kB} \approx 2$ defines the pair creation “wall” for both photon paths, the only difference in escape energies is due to the factor of $\sin \theta_{kB}$ at the front of the pair creation rates in equations (6)–(9). Hence, at the point of pair creation, the value of $\sin \theta_{kB}$ is smaller for the $\theta_{kB,0} = 0.57^\circ$ case, and therefore the escape energy is larger. In flat spacetime, which is not depicted in Figs. 5 or 6, the crossover point of the $\sin \theta_{kB}$ curves occurs at the same s/R value as pair threshold, so that the escape energies are the same at this colatitude for the two cases (this situation was also observed by Chang, Chen and Ho 1996). Note that as photon splitting does not have the same sudden onset as pair creation, it takes place over a range of path lengths, mostly around $0.1 \lesssim s/R \lesssim 2$. Over this range,

$\sin \theta_{kB}$ in Fig. 6 is generally larger for the $\theta_{kB,0} = 0.57^\circ$ case so that the splitting escape energy is correspondingly shorter than for emission parallel to the field, as is evident in Fig. 5a.

3. CASCADE SPECTRA

Here we describe briefly our Monte Carlo simulation of photon propagation and attenuation via splitting and pair creation in neutron star magnetospheres, together with results for single (Section 3.2) and multiple (Section 3.3) generations of photon splitting.

3.1. Monte Carlo Calculation

We model the spectrum of escaping photons from a cascade above a neutron star polar cap, including both photon splitting and pair production, by means of a Monte Carlo simulation. The free parameters specified at the start of the calculation are the magnetic colatitude θ , the angles θ_k and ϕ_k (see Fig. 1), the spectrum, the height above the surface $z_0 = r - R$ of the photon emission, and the surface magnetic field strength B_0 (note that entities with subscripts ‘0’ designate determination at the stellar surface). From these quantities, and assuming that $\phi = 0$ without loss of generality, we compute the four-vectors of the photon position and momentum that are carried through the computation. Injected photons are sampled from a power-law distribution,

$$N(\varepsilon) = N_0 \varepsilon^{-\alpha}, \quad \varepsilon_{min} < \varepsilon < \varepsilon_{max} \quad (12)$$

Polarization is chosen randomly to simulate unpolarized emission; this can be altered, as desired, for any postulated emission mechanism.

The path of each input photon is traced through the magnetic field, in curved spacetime, accumulating the survival probabilities for splitting, P_{surv}^s , and for pair production, P_{surv}^p , independently:

$$P_{\text{surv}}(s) = \exp\{-\tau(s)\} \quad (13)$$

where

$$\tau(s) = \int_0^s T(\theta_{kB}, \omega) ds' \quad (14)$$

is the optical depth along the path. These survival probabilities implicitly depend on the origin \mathbf{r}_0 of the photon and its energy ε at infinity. In computing the attenuation lengths (Section 2.3), the photon was assumed to split when the survival probability reaches $1/e$, i.e. when equation (11) is satisfied. In the cascade simulation, the photon may either split or pair produce. The fate of each cascade photon is determined as follows: if the combined survival probability, $P_{\text{surv}}^s P_{\text{surv}}^p > \mathfrak{R}_1$, where \mathfrak{R}_1 is a random number between 0 and 1, chosen at the emission point, then the photon escapes; if not, then if the probability that the photon survives splitting but not pair production, $P_{\text{surv}}^s (1 - P_{\text{surv}}^p) / (1 - P_{\text{surv}}^s P_{\text{surv}}^p) > \mathfrak{R}_2$, where \mathfrak{R}_2 is a second random number, then the photon

pair produces; otherwise, the photon splits. When the photon splits, the energy of one of the final photons is sampled from the distribution given in equation (2) and their polarizations are chosen from the branching ratios given in equation (3). The energy of the second photon from the splitting is determined simply from energy conservation, since both final photons are assumed to be collinear in the direction of the parent photon. Each final photon is then followed in the same way as the injected photon, with a call to a recursive procedure that stores photon energies and positions through many generations of splitting. When the photon pair produces, the code does not follow the radiation from the pairs but simply returns to the previous cascade generation. For field strengths typical of gamma-ray pulsars, the pair radiation, most probably synchrotron or inverse Compton, will not contribute significantly at the energies near the escape energy for the cascades where all splitting modes operate. An exception to this may occur for supercritical surface fields, where synchrotron photons acquire most of the energy of their primary electrons. When all splitting modes operate, the number of pair production events is a small fraction of the number of splitting events for $B_0 = 0.7B_{\text{cr}}$. The cascade photons are followed through many generations of splitting until all of the photons either escape or pair produce. The escaping photons are binned in energy and polarization.

3.2. Partial Splitting Cascade

For pulsar applications with subcritical fields, as discussed in Section 2.1, it is probable that the splitting modes allowed by CP invariance are further limited by kinematic selection rules to only the $\perp \rightarrow \parallel \parallel$ mode. This restriction may be confined to regimes of weak vacuum dispersion and may also depend on subtleties such as field non-uniformity. Such selection rules would effectively prevent splitting cascades since \perp photons could split only into \parallel photons which do not split. Here we compute the emergent spectra in this type of cascade, a partial cascade, where \perp mode photons can either pair produce or split into \parallel mode photons, while the \parallel mode photons may only pair produce. There is a limit of two cascade generations: one splitting and one pair production. The input spectrum is a power-law (Eq. [12]) with the parameters: $\varepsilon_{\text{min}} = 10^{-3}$, $\varepsilon_{\text{max}} = 100$ and $\alpha = 1.6$. The value of the index α is chosen to match the power-law fit of the OSSE spectrum of PSR1509-58 (Matz et al. 1994). The maximum energy of the input spectrum $\varepsilon_{\text{max}} = 100$ is chosen to fall above the 30 MeV maximum possible cutoff or turnover energy of the observed PSR1509-58 spectrum. For these runs, injection of 5 - 10 million photons are required to give adequate statistics. The number of pairs produced relative to photons in these partial splitting cascades is obviously higher than in the full cascades examined in the next section. Note that in more complete gamma-ray pulsar models that include the pair radiation, multiple generations of splitting might still be possible, being interspersed with generations of conventional synchrotron/pair cascading.

Figure 7 shows partial splitting cascade spectra in each final polarization mode for photons injected parallel to the local magnetic field at different magnetic colatitudes. The spectra for the two polarization modes are cutoff at slightly different energies, reflecting the different escape energies for

splitting, which cuts off the \perp mode, and for pair production, which cuts off the \parallel mode. There is a slight bump below the cutoff in the \parallel mode spectrum, due to escaping photons from $\perp \rightarrow \parallel\parallel$ mode splitting, but only an attenuation cutoff in the *perp* mode spectrum. Figure 8 illustrates the effect of injecting photons at an angle (in this case $\theta_{kB,0} = 0.57^\circ = 0.01$ radians) to the local magnetic field direction, toward the magnetic dipole axis. The high-energy cutoff decreases, compared to the case of injection parallel to the field, only in the \perp mode spectrum and not at all in the \parallel mode spectrum. This behavior is due to the existence of a threshold for pair production, but not for splitting and can be seen from Figs. 5a and 5b. For field strengths well above $B' = 0.1$, where photons pair produce at threshold, the pair escape energy is much less sensitive to increases in $\theta_{kB,0}$ than is the splitting escape energy. The partial cascade spectra therefore become more highly polarized at small colatitudes when $\theta_{kB,0}$ is increased.

This effect of strong polarization, both in the energy of the spectral cutoffs and the spectral shape just below the cutoffs, all but disappears when photon splitting is omitted from the calculation, thereby defining a characteristic signature of the action of $\gamma \rightarrow \gamma\gamma$. Pair production has much less distinctive polarization features. For example, from equations (8) and (9), the ratio of the cutoff energies at pair creation threshold between the polarization states is $(1 + \sqrt{1 + 2B'})/2$. For surface fields of $B' = 0.7$, threshold is crossed during photon propagation in regions with much lower fields, typically $B' \sim 0.1$, so that the spectral cutoff (or escape energy) differs only by about 5% between polarizations; such a difference would be virtually invisible in the emission spectra. Clearly then, splitting is primarily responsible for polarization features shown.

3.3. Full Splitting Cascade

We now present model cascade spectra for the case where all three photon splitting modes allowed by CP invariance, $\perp \rightarrow \parallel\parallel$, $\perp \rightarrow \perp\perp$ and $\parallel \rightarrow \perp\parallel$, are operating, and multiple generations of splitting can occur. These cascades also allow for pair production by photons of either mode. As noted above, for the field strength of $B'_0 = 0.7$ used in the spectral models for PSR1509-58, pair production occurs in less than 10% of conversions.

Figure 9 shows full splitting cascade spectra in each final polarization mode for 2 million photons injected parallel to the local magnetic field (in curved spacetime) at different magnetic colatitudes. Each cascade spectrum shows a cutoff at roughly the splitting escape energy for that colatitude (compare to Fig. 3), and a bump below the cutoff from the escaping cascade photons. The size of the bump is a function of the number of photons attenuated above the cutoff, which is dependent on the ratio of the maximum input energy, ε_{max} , and the escape energy. For these models, the size of the cascade bump grows with increasing θ because ε_{max} is held constant while the escape energy is decreasing. The number of splitting generations ranges from 12 when $\theta = 30^\circ$ to 3 when $\theta = 2^\circ$. The size of the cascade bump at a particular θ could of course be larger or smaller if ε_{max} were increased or decreased, but the positions of the cutoffs would not vary. The spectrum of the bump is polarized, with a well-defined zero in polarization that is a characteristic signature

of the splitting cascade (see Baring 1995). Note that the polarization modes have reversed their flux dominance in the cascade bump compared to the partial splitting cascade case.

Although we have injected unpolarized photons in these calculations for simplicity, the relative flux (i.e. spectra integrated over energies) of the two polarization modes generally has a complicated dependence on the branching ratios for splitting defined by equation (3), due to the cascading process and the non-uniformity of the field. Notwithstanding, the polarization at a given energy does not exceed a limiting value of 3/7 (Baring 1991). The cascade spectra for injection of polarized photons resemble the spectra in Fig. 9, though deviations from Fig. 9 are not exactly proportional to the degree of polarization of the injection spectrum due to the inherent complexity of the interplay of polarization states in the cascade.

As shown in Figure 10, injecting photons at an angle to the local field again has a much larger effect at small colatitudes (i.e. for $\theta \lesssim 100\theta_{kB,0}$). The high-energy cutoffs in both modes now decrease in energy compared to the case of injection parallel to the field, and the sizes of the cascade bumps are larger, both being consequences of decrease in escape energy (see Fig. 5a). This effect is larger at smaller colatitudes.

4. PHOTON SPLITTING CASCADE MODELS FOR PSR1509-58

The multiwavelength spectrum of PSR1509-58, compiled from radio to TeV energies (Thompson 1996), shows that the peak in the power output from this pulsar, as is the case for most other γ -ray pulsars, falls in the γ -ray band. Figures 11–14 show the high energy portion of this spectrum, near the cutoff, which we compare with our model spectra at different emission colatitudes. No formal procedure for fitting the data with the model was followed, since a simple visual comparison demonstrating the spectral cutoff is sufficient for the scientific goals of this paper. The $\epsilon^2 F(\epsilon)$ format plots equal energy per logarithmic decade and clearly demonstrates the need for a cutoff or sharp turnover somewhere between the highest OSSE detected point at 3 MeV and the lowest EGRET upper limit at 30 MeV. Although there appears to be a discontinuity between the GINGA data points below 100 keV and the OSSE data points, it is common for separate fits of data from two different detectors to produce disparate results, even in the same energy range. Furthermore, the $\epsilon^2 F(\epsilon)$ format tends to magnify the differences. The difference in spectral index of the Ginga and OSSE fits probably indicates a true break in the power-law spectrum around 100 keV. We have taken the OSSE index for the input spectrum for our cascade simulation since it most accurately measures the observed spectrum at the energies of importance for the model. The offset between the Ginga and OSSE data (or their different spectral indices) does not impact the conclusions of this paper, since the cascade formation is determined by the photon population in the upper end of the OSSE range. Note that while EGRET has obtained upper limits to the pulsed emission above around 30 MeV, there are earlier reports of a marginal detection by COS-B (e.g.. Hartmann et al. 1993), with data points lying above the EGRET limits. This apparent discrepancy remains to be resolved, and we opt here to consider only the later and superior EGRET observations. The

Comptel point and limits in Figs. 11–14 are a preliminary analysis of data from VP23 (Hermsen et al. 1996), showing pulsed flux at 0.75 - 1 MeV and upper limits for the pulsed interval (50%) of the light curve.

The cutoffs in the model photon splitting cascade spectra in Figures 11–14 do in fact fall in the energy range 3–30 MeV for colatitudes less than around 30° . At colatitudes greater than $\sim 30^\circ$ the cutoffs are lower and are in severe conflict with the OSSE data points. The standard polar cap half-angle in flat spacetime, $\sin \theta = (\Omega R/c)^{1/2}$, for PSR1509-58 is 2.14° . Although curved spacetime corrections to the magnetic dipole field tend to very slightly decrease the polar cap size (GH94), the polar cap may be larger than the standard size due to distortion of the field near the light cylinder by plasma loading (Michel 1991). The results presented here assume, for simplicity, a single colatitude of emission for each, i.e. a polar rim rather than an extended cap. It is easy to envisage that a range of polar cap emission locations will produce a convolution of the spectra presented here, thereby generating a spectral turnover corresponding to the maximum colatitude of the cap, with steeper emission extending up to a cutoff defined by the minimum colatitude. The EGRET upper limits cannot really discern between a sharp cutoff or a more modest turnover above the Comptel energy range and so cast little light on the emission as a function of colatitude when $\theta \lesssim 2^\circ$.

The partial splitting cascade spectra, shown in Figs. 11 and 12, exhibit only modest cascade bumps just below the cutoff. The limits on colatitude of the model spectra are essentially determined by the cutoff energy and are restricted by the lowest EGRET upper limit to $2^\circ \lesssim \theta \lesssim 25^\circ$ in the $\theta_{kB,0} = 0$ case, and $\theta \lesssim 25^\circ$ in the $\theta_{kB,0} = 0.57^\circ$ case, where no lower limit to the colatitude is imposed by the observations (see below). The model spectra for $\theta = 2^\circ$ and 5° are only marginally consistent with the upper limits. The final revision of the Comptel data for PSR1509-58 (Bennett et al., in preparation) may require raising the lower bounds to the colatitude of emission obtained in this model/data comparison. The cutoff energies of these polarization-averaged spectra are somewhat larger than the cutoff energies of the full cascade spectra (see Figs. 13 and 14) because the \parallel mode escape energies are determined solely by pair production, whose escape energies generally exceed those of splitting at this field strength (see Fig. 3). This is especially pronounced in the $\theta_{kB,0} = 0.57^\circ$ case, due to the fact that the pair production escape energy is insensitive to the photon emission angle for $B \gg 0.1$, as is illustrated in Fig. 5b.

The full cascade spectra, shown in Figs. 13 and 14, have distinctive bumps below the cutoff due to the redistribution of photon energies via splitting. The size of the cascade bump further limits the magnetic colatitudes to $\theta \lesssim 5^\circ$ to avoid conflict with the Comptel upper limits. The lowest EGRET upper limit restricts the colatitudes to $5^\circ \gtrsim \theta \gtrsim 2^\circ$ in the case of emission parallel to the field (Fig. 13). In the case of emission at angle $\theta_{kB,0} = 0.57^\circ$ (Fig. 14), the cutoff energy in the cascade spectra saturates at small θ at an energy of 25 MeV (see Fig. 5a). Consequently there is no low-energy limit to θ in this case. For larger values of $\theta_{kB,0}$, the spectral cutoffs would saturate at larger values of θ and at lower energies. We can estimate the dependence of this saturation escape energy, ε_{esc}^{sat} , on $\theta_{kB,0}$ and B' using the expression for the splitting attenuation coefficient in

equation (1). Assuming that $1/T_{\text{sp}} \simeq R$ approximately gives the escape energy:

$$\varepsilon_{\text{esc}}^{\text{sat}} \simeq 0.077 (B' \sin \theta_{\text{kB},0})^{-6/5}, \quad B' \lesssim 0.3. \quad (15)$$

This formula quite accurately reproduces the escape energies in Figs. 13 and 14 since they are only weakly dependent on R , specifically $\varepsilon_{\text{esc}}^{\text{sat}} \propto R^{-1/5}$. When $\varepsilon_{\text{esc}}^{\text{sat}} \leq 7.8$ (i.e. 4 MeV), cascade spectra at all colatitudes cutoff below the lowest possible observed cutoff energy for the PSR1509-58 spectrum. From equation (15), this occurs, for surface emission, at $\theta_{\text{kB},0} \gtrsim 0.03$ for $B'_0 = 0.7$. Therefore, splitting cascade spectra from photons emitted at larger angles to the field will not be compatible with the spectrum of PSR1509-58. For emission at some distance above the surface, the limit on $\theta_{\text{kB},0}$ would be higher since it depends inversely on local field strength.

All the model spectra in Figures 11–14 assume emission at the neutron star surface. Emission above the surface would produce higher cutoff energies at a given colatitude, due to the decrease in the dipole field strength with r . The upper limits on colatitude stated above would therefore be less restrictive for non-surface emission. Furthermore, when the field strength at the emission point is $B \sim 0.3B_{\text{cr}}$ (at height 30% of the neutron star radius) the splitting and pair production escape energies are comparable, reducing the size of the splitting cascade bumps in all cases. At higher altitudes above the surface, pair production dominates the photon attenuation and conventional pair cascades (e.g. Daugherty & Harding 1996) would operate. Synchrotron radiation from the pairs would then result in a significantly softer emergent spectrum than the input power-law above the cyclotron energy ($\sqrt{1+2B'} - 1 \approx 280$ keV at the stellar surface, lower at greater radii). Consequently, in order to match the observations, the input power-law would have to be harder, and because of the remoteness of the emission point from the stellar surface, the colatitude θ of emission would have to be increased substantially.

5. DISCUSSION

The results of this paper demonstrate that magnetic photon splitting can have a significant effect on γ -ray emission from the higher field ($B_0 \gtrsim 10^{13}$ G) pulsars. It can attenuate the γ -ray spectrum at lower energies than magnetic pair production and will do so without the creation of electron-positron pairs. We have found that in low fields ($B_0 \lesssim 0.3B_{\text{cr}}$) and $\theta_{\text{kB},0} = 0$ initially, photon splitting attenuation lengths are never shorter than those for pair production. In high fields ($B_0 \gtrsim 0.3B_{\text{cr}}$), photon splitting lengths fall below those for pair production below a certain energy which depends on the colatitude θ . Photon splitting escape energies fall below pair production escape energies for $B_0 \gtrsim 0.5B_{\text{cr}}$, so that splitting may produce an observable signature for γ -ray pulsars having strong magnetic fields: high energy spectral cutoffs that are quite polarization-dependent. While pair creation alone will also generate such cutoffs, their dependence on photon polarization is far diminished from when splitting is active.

We have modeled the shape of such spectral cutoffs through simulation of photon splitting cascades near the neutron star surface for the case of PSR1509-58. Two types of cascades result

from different assumptions about the selection rules governing the photon splitting modes: the “full splitting cascades” occur when three modes limited only by CP selection rules operate and the “partial splitting cascades” occur when only one mode permitted by kinematic selection rules operates. In the full cascades, splitting dominates the attenuation while in the partial cascades, pair production ultimately limits the rate at which photon energy degrades. However, the partial cascades show a distinct polarization signature due to the different escape energies for splitting and for pair production. The resulting PSR1509-58 model spectral cutoffs due to splitting and pair production fall in the required range for virtually all colatitudes $\lesssim 25^\circ$. However, the shape of the spectrum of full splitting cascades, due to the large reprocessing bump, is compatible with the data only for a very small range of colatitudes, $\theta \lesssim 5^\circ$. From these results we conclude that, although photon splitting is capable of producing spectral cutoffs well below EGRET energies regardless of which selection rules govern the splitting modes, the partial splitting cascades have a much larger range of phase space in which to operate.

Attenuation through magnetic pair production and photon splitting near the polar cap will produce γ -ray spectral cutoffs that should be roughly a function of surface magnetic field strength, although other parameters such as polar cap size will come into play. Thus the γ -ray pulsar PSR0656+14, having the second highest surface field of 9.3×10^{12} G, should have a cutoff energy between that of PSR1509-58 and the other γ -ray pulsars. In fact the unusually large spectral index of 2.8 measured by EGRET (Ramanamurthy et al. 1996) may be a pair production/photon splitting cutoff.

It is thus possible to understand why PSR1509-58, with the highest magnetic field of all the γ -ray pulsars, has by far the lowest spectral cutoff energy and is the only γ -ray pulsar not detected by EGRET. In the case of Vela (Kanbach et al. 1994), Geminga (Meyer-Hasselwander et al. 1994) and 1055-52 (Fierro et al. 1993), the spectral cutoffs observed by EGRET at a few GeV are consistent with one-photon pair production cascades (Daugherty and Harding 1982, 1996). Although the escape energies at the neutron star surface for the spin-down fields of these pulsars ($B_0 \sim 2-6 \times 10^{12}$ G) is below 1 GeV (see Fig. 5a), curvature radiation from primary electrons at one to two stellar radii above the surface will have pair production escape energies of several GeV. However, when the surface field exceeds $\sim 10^{13}$ G, photon splitting becomes the dominant attenuation mechanism in the electromagnetic cascades. In addition, the primary electrons may lose energy to resonant Compton scattering of thermal X-rays from the neutron star surface (Sturner 1995), rather than to curvature radiation, limiting their acceleration to much lower energies, typically $\gamma \sim 100$. The resulting upscattered γ -ray spectrum is radiated much closer to the surface and will be cut off by photon splitting well below the EGRET energy range. It is important to emphasize that pair creation acting alone suffices to inhibit GeV emission in pulsars with spin-down fields as high as PSR1509-58, and splitting significantly enhances the attenuation and pushes spectral cutoffs to lower energies.

If resonant Compton scattering losses limit the polar cap particle acceleration energies to $\gamma \ll 10^6$ when $B \gtrsim 10^{13}$ G, then the primary particles will radiate γ -rays via the cyclotron

upscattering process or CUSP (Dermer 1990). CUSP radiation would then provide the seed photons for the splitting cascade. The γ -ray spectrum for this process for power-law and monoenergetic electrons scattering thermal blackbody X-ray photons above the neutron star surface (Daugherty & Harding 1989) is a power-law with maximum energy $\varepsilon_{max} \simeq \gamma_c B' = 2 \times 10^3 B'^2/T_6$ (Dermer 1990), where γ_c is the energy above which the electrons scatter resonantly and $T_6 \equiv T/10^6$ K is the thermal X-ray temperature. In the case of PSR1509-58 with $B' = 0.7$, $\varepsilon_{max} \simeq 10^3/T_6$. Since the thermal surface emission component is not observed due to the strong non-thermal spectrum seen at X-ray energies (Kawai 1993), T_6 is not known. However, PSR1509-58 is young (~ 1000 yr) and probably has $T_6 \sim 1 - 3$. We would then expect $\varepsilon_{max} \simeq 300 - 10^3$, compatible with our choice of $\varepsilon_{max} = 100$ for the splitting cascade models.

A dozen or so other radio pulsars have spin-down magnetic fields above 10^{13} G. These pulsars would, like PSR1509-58, have photon splitting dominated cascades rather than pair cascades, producing lower yields of electron-positron pairs. It is possible that neutron stars with extremely high magnetic fields, where splitting is dominant at altitudes up to several stellar radii, do not produce sufficient pairs for coherent radio emission, an intriguing possibility. If such neutron stars exist, they would constitute a new class of radio quiet, low-energy γ -ray pulsars.

We thank Dieter Hartmann and David Thompson for reading the manuscript and for providing helpful comments, and Wim Hermsen, Alberto Carramiñana and Kevin Bennett for providing preliminary Comptel data for PSR1509-58. This work was supported through Compton Gamma-Ray Observatory Guest Investigator Phase 5 and NASA Astrophysics Theory Grants. MGB thanks the Institute for Theoretical Physics at the University of California, Santa Barbara for support (under NSF grant PHY94-07194) during part of the period in which work for this paper was completed.

A. CURVED SPACETIME EFFECTS

We include here some details of our treatment of general relativistic effects on the photon splitting and pair production attenuation in a neutron star magnetosphere. This treatment follows closely that of Gonthier & Harding (1994), who examined the importance of general relativistic effects on one-photon pair production attenuation in a Schwarzschild metric. They found that several effects of curved spacetime make significant corrections to the attenuation lengths and escape energies for this process, namely the curvature of the photon trajectories, the redshift of the photon energy, and the change in the dipole magnetic field. In the present calculation, the first two effects are included together in the expression for the photon momentum 4-vector. The curved trajectory of a photon in the Schwarzschild metric is confined to a single plane, which we may specify as the x-z plane. For an observer at rest in the local inertial frame at a radius r in the Schwarzschild field, the components of the momentum 4-vector are then

$$\begin{aligned} k^{\hat{r}} &= \left[(1 - 2u)^{-1} - \frac{u^2}{u_b^2} \right]^{1/2} \varepsilon \\ k^{\hat{\vartheta}} &= \frac{u}{u_b} \varepsilon \\ k^{\hat{\phi}} &= 0 \\ k^{\hat{o}} &= (1 - 2u)^{-1/2} \varepsilon \quad , \end{aligned} \quad (\text{A1})$$

where $u = m/r$, with $m = GM/c^2$ as the scaled stellar mass (i.e. the Schwarzschild radius), ε is the photon energy as observed at infinity,

$$u_b = \frac{m}{R \sin \delta_o} \sqrt{1 - \frac{2m}{R}} \quad (\text{A2})$$

for a neutron star radius of R , and δ_o is the initial propagation angle of the photon to the radial direction. The $\hat{\vartheta}$ and \hat{o} components of k are adapted from equations (13) and (14) of Gonthier & Harding (1994), $k^{\hat{\phi}} = 0$ follows from the choice of the plane of propagation, and the \hat{r} component can be deduced from the others using $k_\mu k^\mu = 0$.

At the photon emission point, we first determine the angle δ_o by performing two coordinate transformations to put the photon momentum 3-vector in the x-z plane. The spacetime trajectory for that photon is then computed and stored in two tables: the first giving the value of r as a function of the total pathlength along the trajectory, $s = c\Delta\tau$, from the time-of-flight in the local frame,

$$\Delta\tau = -\frac{m}{c} \int_{m/R}^{m/r} \frac{u_b du}{[u_b^2 - u^2(1 - 2u)]^{1/2} (1 - 2u)^{1/2} u^2} \quad , \quad (\text{A3})$$

which closely resembles Eq. (19) of Gonthier and Harding (1994, which instead measures time in the non-local observer's frame), and the second table giving the value of ϑ as a function of r from the equation,

$$\left(\frac{du}{d\vartheta} \right)^2 = u_b^2 - u^2(1 - 2u) \quad . \quad (\text{A4})$$

The r and ϑ are the coordinates in the x-z plane of each point along the photon trajectory. At each distance s along the photon path from the emission point, we look up the value of r , and from r deduce the value of ϑ . These values of r and ϑ then define the new position and momentum 4-vectors in the x-z plane. The inverse coordinate transformations of those described above will then give the position and momentum 4-vectors in the frame in which we carry out the attenuation length calculation.

To describe the magnetic field in curved spacetime, we use the expression of Wasserman & Shapiro (1983) for the dipole field measured in the local inertial frame in a Schwarzschild metric:

$$\vec{B}_{curved} = -\frac{3}{2} \frac{B_0 \cos \vartheta}{m^2 r} \left[\frac{r}{2m} \ln \left(1 - \frac{2m}{r} \right) + 1 + \frac{m}{r} \right] \hat{r} + \frac{3}{2} \frac{B_0 \sin \vartheta}{m^2 r} \left[\left(\frac{r}{2m} - 1 \right) \ln \left(1 - \frac{2m}{r} \right) + 1 - \frac{m}{r} \right] \left(1 - \frac{2m}{r} \right)^{-1/2} \hat{\vartheta} . \quad (A5)$$

Note that this expression in GH94 has a typographical error in the $\hat{\vartheta}$ component. For $M = 1.4M_\odot$ and $R = 10$ km, as used in this paper, the dipole field strength at the neutron star surface at the pole from equation (A5) is a factor ~ 1.4 times the flat space value.

The angle θ_{kB} , obtained by taking the dot product between the photon momentum 4-vector and the local dipole field, is given in curved spacetime by

$$\cos \theta_{kB} = \frac{B^{\hat{r}}}{B} \left[1 - (1 - 2u) \frac{u^2}{u_b^2} \right]^{1/2} + \frac{B^{\hat{\vartheta}}}{B} \frac{(1 - 2u)^{1/2} u}{u_b} . \quad (A6)$$

Since the field components $B^{\hat{r}}$ and $B^{\hat{\vartheta}}$ defined by $\vec{B}_{curved} = B^{\hat{r}} \hat{r} + B^{\hat{\vartheta}} \hat{\vartheta}$ in equation (A5) are differentiable functions of $u = m/r$, it follows from equation (A6) that θ_{kB} is also differentiable in r . Note also that the pathlength s defined through equation (A3) gives smooth $\partial s / \partial r$ at all positions above the stellar surface. Consequently, the implicit function $\theta_{kB}(s)$ has a well-behaved Taylor series expansion (i.e. there is no singularity) about $r = R$ (i.e. $s = 0$). Hence, cases where we set $\theta_{kB,0} = 0$ result in $\theta_{kB} \propto s$ along the photon trajectory for $(r - R)/R \ll 1$, regardless of whether the spacetime is curved or flat. This proportionality is responsible for certain limiting behaviors in the attenuation lengths and escape energies discussed in Sections 2.3 and 2.4.

REFERENCES

Adler, S. L., 1971, Ann. Phys., 67, 599.

Adler, S. L., Bahcall, J. N., Callan, C. G., & Rosenbluth, M. N.: 1970 Phys. Rev. Lett., 25, 1061.

Arons, J. 1983, ApJ, 266, 215.

Baring, M. G. 1988, MNRAS, 235, 79.

Baring, M. G.: 1991 A&A, 249, 581.

Baring, M. G.: 1993 MNRAS, 262, 20.

Baring, M. G. 1995, ApJ, 440, L69.

Baring, M. G. & Harding, A. K., 1995a, Ap&SS, 231, 77.

Baring, M. G. & Harding, A. K., 1995b, Proc. of 24th Intl. Cosmic Ray Conf., Vol. II, p. 271.

Baring, M. G. & Harding, A. K., 1996, ApJ Letters, submitted.

Baier, V. N., Mil'shtein, A. I., & Shaĭsultanov, R. Zh 1986, Sov. Phys. JETP, 63, 665.

Baier, V. N., Mil'shtein, A. I., & Shaĭsultanov, R. Zh 1996. Phys. Rev. Lett., 77, 1691.

Bennett, K. et al., 1994, ApJS, 90, 823.

Bertsch, D. L. et al. 1992, Nature, 357, 306.

Bialynicka-Birula, Z., & Bialynicki-Birula, I. 1970, Phys. Rev. D, 2, 2341.

Bulik, T. & Miller, M. C. 1996, preprint.

Chang, H.-K., Chen, K., Fenimore, E. E., & Ho., C. 1996, Proc. Huntsville Workshop on Gamma-Ray Bursts, (AIP, New York) in press.

Chang, H.-K., Chen, K., & Ho., C. 1996, A&A, in press.

Cheng, K. S., Ho, C. & Ruderman, M. A. 1986, ApJ, 300, 500.

Chiang, J. & Romani, R. W. 1992, ApJ, 400, 629.

Daugherty, J. K. & Harding A. K., 1982, ApJ, 252, 337.

Daugherty, J. K. & Harding, A. K. 1983, ApJ, 273, 761. (DH83)

Daugherty, J. K. & Harding A. K., 1994, ApJ, 429, 325.

Daugherty, J. K. & Harding A. K., 1996, ApJ, 458, 278.

Fierro, J. M. et al. 1993, ApJ, 413, L27.

Gonthier, P. L. & Harding, A. K., 1994, ApJ, 425, 767.

Halpern, J. P. & Holt, S. S. 1992, Nature, 357, 222.

Harding, A. K. 1995, in *Milisecond Pulsars: A Decade of Surprises*, ed. A. S. Fruchter, M. Tavani & D. C. Backer (ASP Conf. Proc. Vol. 72), p. 322.

Harding, A. K. & Baring, M. G. 1996, Proc. Huntsville Workshop on Gamma-Ray Bursts, (AIP, New York) in press.

Harding, A. K., Baring, M. G. & Gonthier, P. L. 1996, A&A, in press.

Hartmann, D. H. et al., 1993, in *Isolated Pulsars*, ed. K. van Riper, R. Epstein & C. Ho, Cambridge Univ. Press, p. 405.

Hermsen, W. et al. 1996, Adv. Space Research, in press.

Jauch, M. M., & Rohrlich, F. 1980, *The Theory of Photons and Electrons* (2nd edn. Springer, Berlin).

Kanbach, G. et al. 1994, A&A, 289, 855.

Kawai, N., Okayasu, R. & Sekimoto, Y. 1993, in *Compton Gamma-Ray Observatory*, eds. M. Friedlander, N. Gehrels, D. J. Macomb (AIP Conf. Proc. 280, AIP, New York) p. 213

Klepikov, N. V. 1954, Zh. Eksp. Theor. Fiz., 26, 19.

Manchester, R. N. & Taylor, J. H., 1977, *Pulsars* (Freeman, San Francisco).

Matz, S. M. et al. 1994, ApJ, 434, 288.

Mayer-Hasselwander, et al. 1994, ApJ, 421, 276.

Melrose, D. B., & Parle, A. J. 1983a, Aust. J. Phys., 36, 775

Melrose, D. B., & Parle, A. J. 1983b, Aust. J. Phys., 36, 799

Mentzel, M., Berg, D & Wunner, G. 1994, Phys. Rev. D, 50, 1125.

Michel, F. C., 1991, *Theory of Neutron Star Magnetospheres* (Univ. of Chicago Press).

Minguzzi, A. 1961, Nuovo Cimento, 19, 847.

Mitrofanov, I. G., Pozanenko, A. S., Dolidze, V. Sh., Barat, C., Hurley, K., Niel, M., & Vedrenne, G. 1986, Sov. Astron, 30, 659.

Nel, H. I. et al. 1992, ApJ, 398, 602.

Nel, H. I. et al. 1996, ApJ, in press.

Nolan, P. L. et al. 1993, ApJ, 409, 697.

Papanyan, V. O. & Ritus, V. I., 1972, Soviet JETP, 34, 1195.

Ramanamurthy, P. V. et al. 1995, ApJ, 447, L109.

Ramanamurthy, P. V. et al. 1996, ApJ, in press.

Romani, R. W. & Yadigaroglu, I.-A. 1995, ApJ, 438, 314.

Ruderman, M. A. & Sutherland, P. G. 1975, ApJ, 196, 51.

Shabad, A. E. 1975, Ann. Phys., 90, 166.

Shapiro, S. L. & Teukolsky, S. A., 1983, Black Holes, White Dwarfs, and Neutron Stars: The Physics of Compact Objects (John Wiley & Sons: New York), 278.

Stoneham, R. J., 1979, J. Phys. A 12, 2187.

Sturner, S. J. 1995, ApJ, 446, 292.

Sturner, S. J. & Dermer, C. D., 1994, ApJ, 420, L79.

Sturrock, P. A. 1971, ApJ, 164, 529

Thompson. D. J. et al. 1992, Nature, 359, 615.

Thompson, D. J. 1996, in Proc. IAU Colloquium 160 (Sydney, Australia), in press.

Toll, J. S. 1952, Ph.D. Thesis, Princeton University.

Tsai, W.-Y. & Erber, T. 1974, Phys. Rev. D, 10, 492.

Usov, V. V. & Melrose, D. B. 1995, Aust. J. Phys., 48, 571.

Usov, V. V., & Shabad, A. E. 1983, Sov. Astron. Lett., 9, 212.

Wasserman, I. & Shapiro, S.L., 1983, ApJ, 265, 1036.

Wilke, C. & Wunner, G. 1996, Phys. Rev. D, submitted.

Wilson, R. B. et al., 1993, in *Isolated Pulsars*, ed. K. van Riper, R. Epstein & C. Ho, Cambridge Univ. Press, p. 257.

Wunner, G., Sang, R., & Berg, D. 1995, ApJ, 455, L51

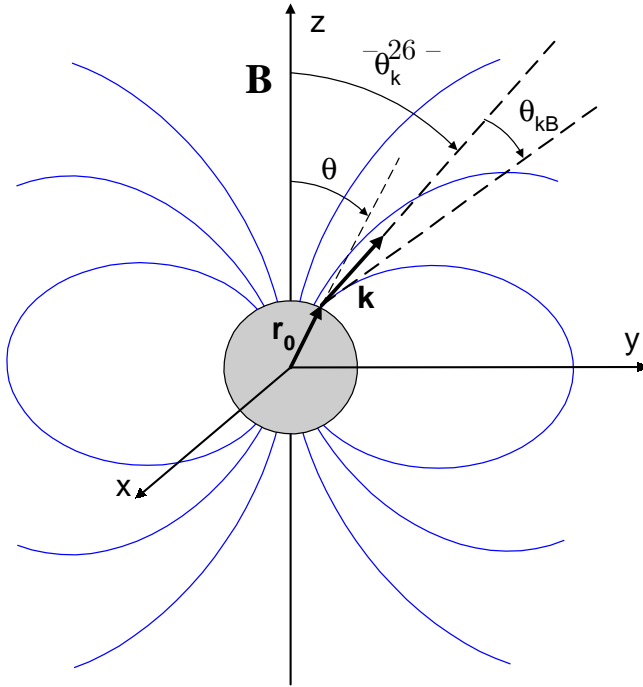


Fig. 1.— Schematic illustration of the neutron star dipole magnetic field geometry, used for determination of attenuation lengths and escape energies. The dipole field has an axis in the z -direction, and the photon originates at position vector \mathbf{r}_0 on the neutron star surface, labelled by the polar angle θ . The photon propagates in the direction of its momentum vector \mathbf{k} that makes an angle θ_{kB} to the local field ($\theta_{kB,0}$ at the emission point), and is described by polar angle θ_k with respect to its original location \mathbf{r}_0 . For all results in this paper, we arbitrarily choose a photon trajectory in x - z plane, corresponding to a phase $\phi = 0$ (see the Appendix).

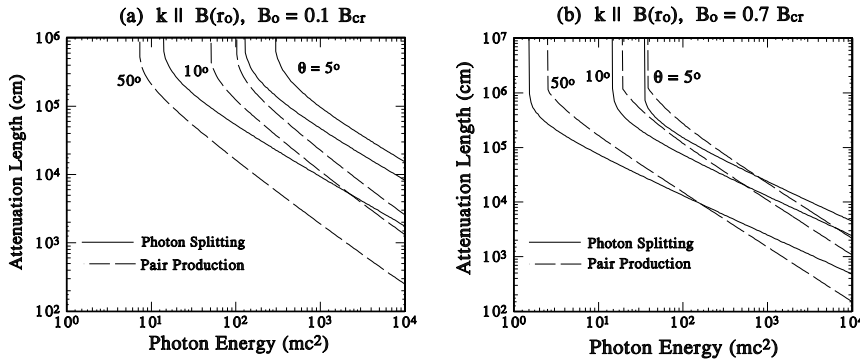


Fig. 2.— The attenuation length L for photon splitting, defined in equation (1) assuming three CP-permitted modes, and for single photon pair production as a function of energy for photons initially propagating parallel to the local field (i.e. $\theta_{kB,0} = 0$), at different colatitudes θ on the neutron star surface. Two cases are depicted, namely for surface fields of (a) $B_0 = 0.1 B_{cr}$ and (b) $B_0 = 0.7 B_{cr}$, the latter being the spin-down field strength for PSR1509-58. At high energies ε , the lengths scale as $\varepsilon^{-5/7}$ for photon splitting and ε^{-1} for pair production, as discussed in the text. The lengths are averaged over photon polarizations.

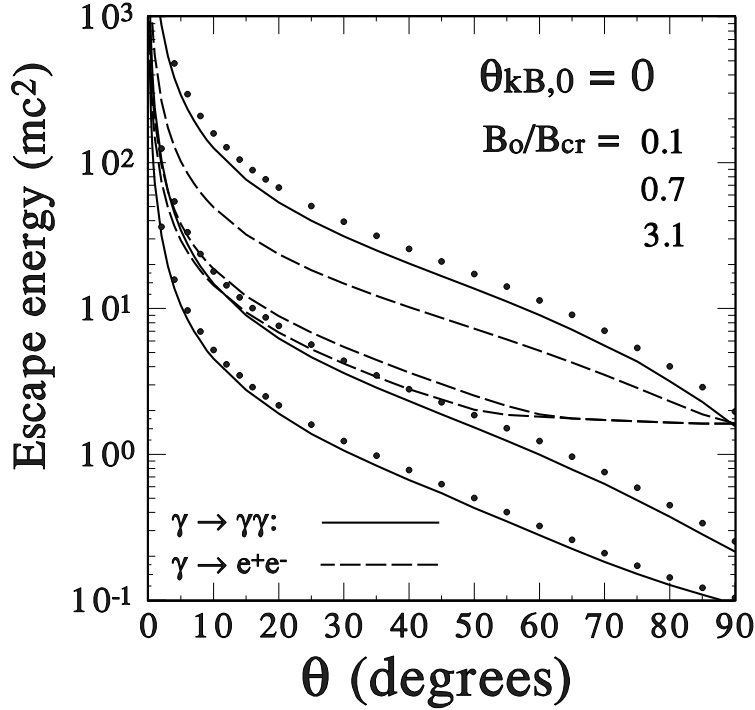


Fig. 3.— The escape energy (i.e. where $L \rightarrow \infty$ in Eq. [11]), in units of $m_e c^2$, for photon splitting, averaged over all modes (solid curves) and in the $\perp \rightarrow \parallel$ mode only (solid dots), compared to the escape energy for one-photon pair production (dashed curves), both as functions of magnetic colatitude θ of the emission point on the neutron star surface. These energies are obtained for three different surface dipole magnetic field strengths and for emission along the field ($\theta_{kB,0} = 0$). The curves diverge near $\theta = 0$, where the field line radius of curvature becomes infinite; these divergences scale as $\theta^{-6/5}$ for splitting and θ^{-1} for pair production (see text and also Fig. 5 below). The escape energies for each process are monotonically decreasing functions of B for the range of parameters shown. The escape energies are averaged over photon polarizations and computed using the Schwarzschild metric.

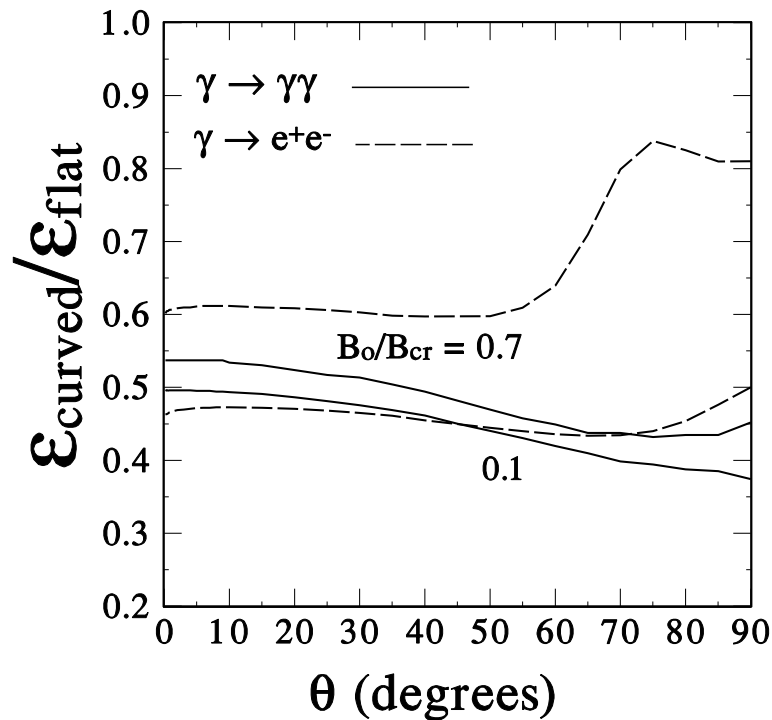


Fig. 4.— The ratio of escape energies in curved and flat spacetime for photon splitting and pair production, for emission parallel to the field as a function of magnetic colatitude θ of the emission point.

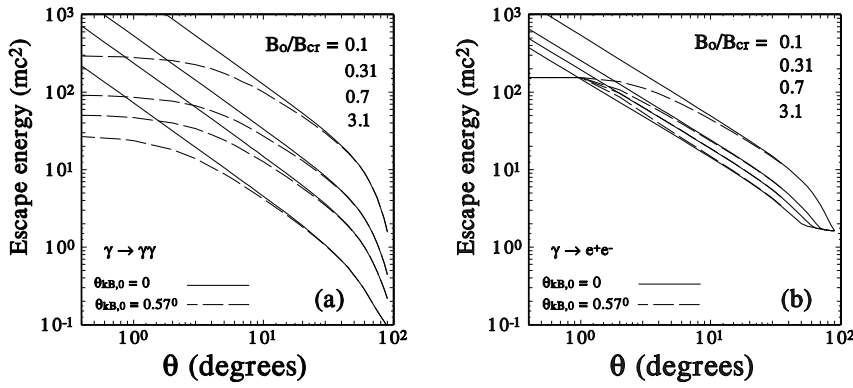


Fig. 5.— The escape energy for (a) photon splitting and (b) pair production as a function of magnetic colatitude for photon emission both along \mathbf{B} and at angle $\theta_{kB,0} = 0.01$ radians ($= 0.57^\circ$) to the field. At low magnetic colatitudes $\theta \lesssim 10\theta_{kB,0}$, the field curvature is so low that photon attenuation is insensitive to the value of θ and is well described by the uniform field results in equations (1) and (7–10). The $\theta_{kB,0} = 0$ (solid) curves have slopes of $-6/5$ (splitting) and -1 (pair creation) at small θ , as discussed in the text.

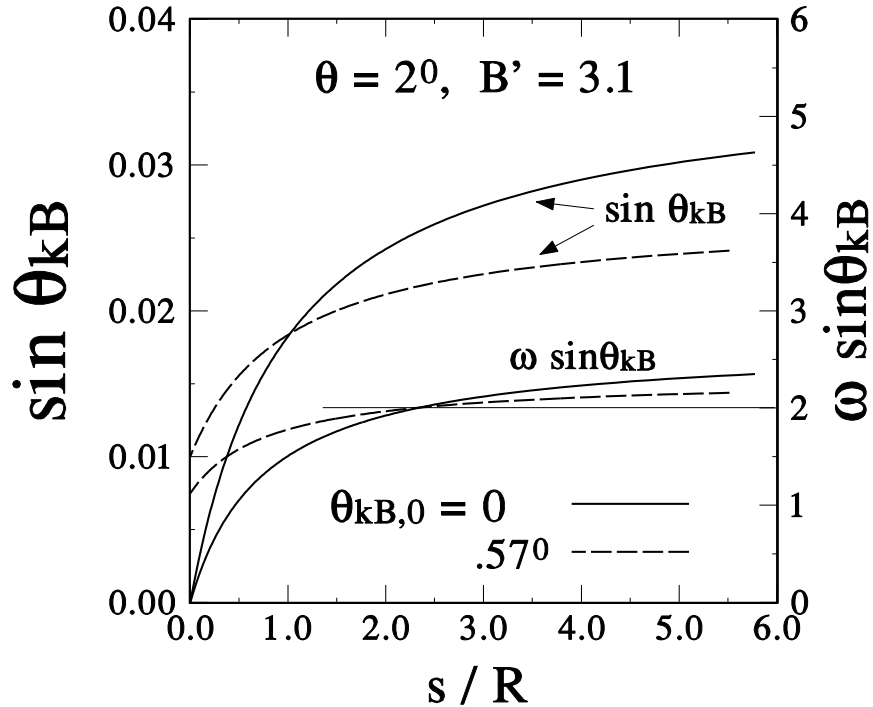


Fig. 6.— The variation of $\sin \theta_{kB}$ (left-hand scale) and $\omega \sin \theta_{kB}$ (right-hand scale) with path length s above the neutron star surface, scaled by the radius R , in curved spacetime for two different values of $\theta_{kB,0}$. ω is the photon energy in the local inertial frame and the light solid horizontal line marks the pair threshold. Observe that $\theta_{kB} \propto s$ for $s/R \ll 1$. The colatitude $\theta = 2^\circ$ and field strength $B' = 3.1$ are chosen specifically to facilitate the understanding of Fig. 5.

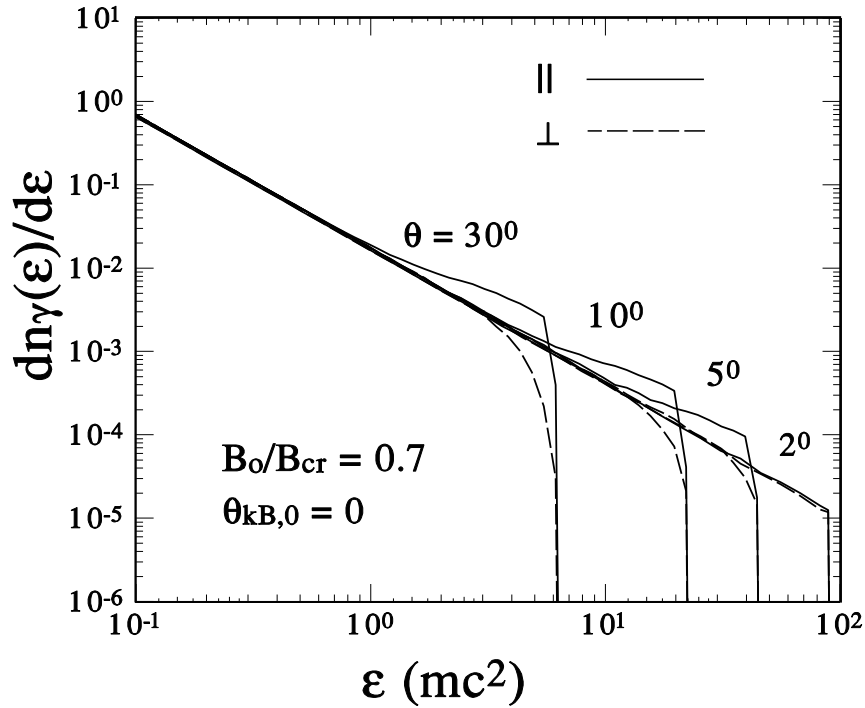


Fig. 7.— Polarized spectra for partial photon splitting cascades, assuming unpolarized power-law emission (of index $\alpha = 1.6$) parallel to the magnetic field ($\theta_{kB,0} = 0$), at different magnetic colatitudes, θ , as labelled. Here only photons of polarization \perp split, while those of either polarization produce pairs. The normalization of the spectrum is arbitrary.

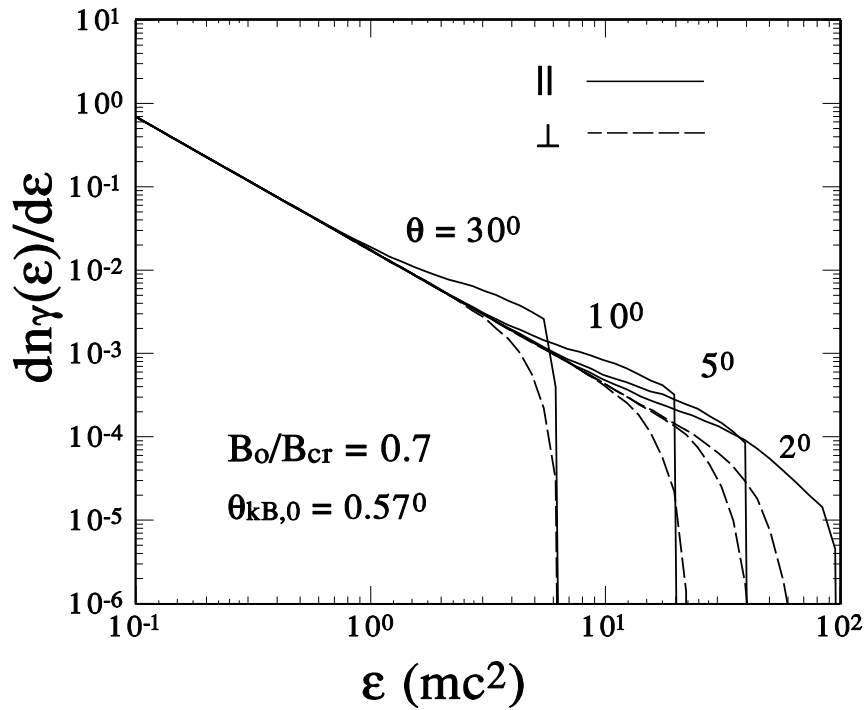


Fig. 8.— Same as Fig. 7, but for emission at angle $\theta_{kB,0} = 0.01$ radians ($= 0.57^\circ$) to the field. Spectra differ only marginally from Fig. 7.

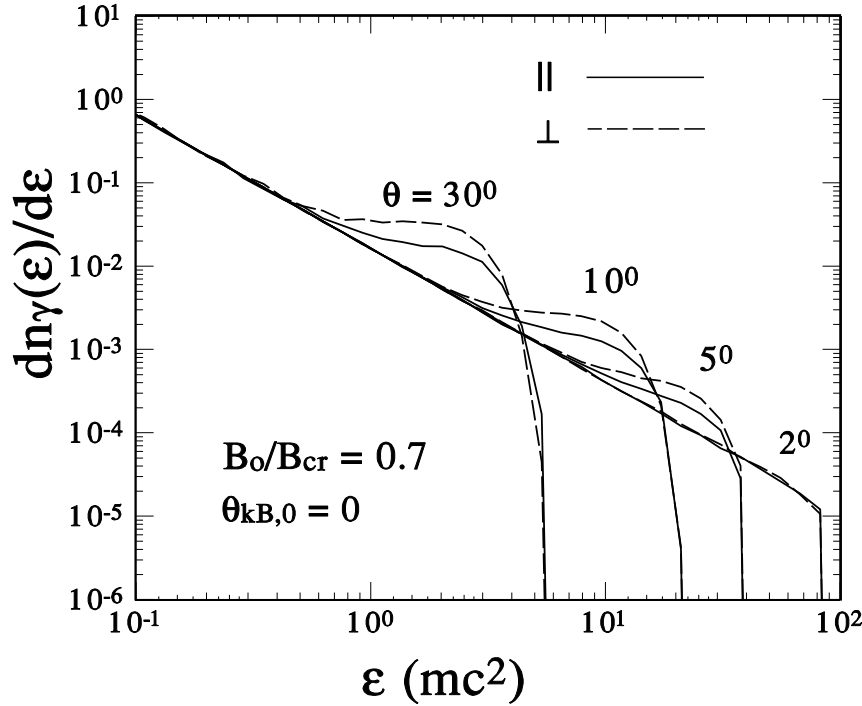


Fig. 9.— Polarized spectra for full photon splitting cascades, assuming unpolarized power-law emission (of index $\alpha = 1.6$) parallel to the magnetic field ($\theta_{kB,0} = 0$), at different magnetic colatitudes, θ . The cutoffs occur at energies comparable to the escape energies computed in Section 2.4. Pair creation is permitted in these runs, and is generally small away from the pole.

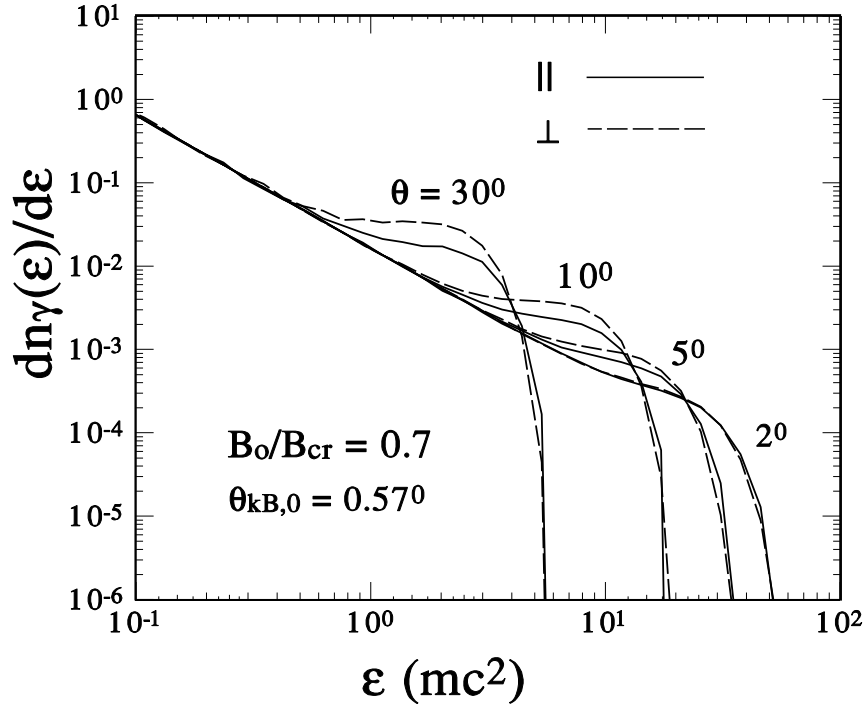


Fig. 10.— Same as Fig. 9, but for emission at angle $\theta_{kB,0} = 0.57^\circ$ to the field, towards the dipole axis. This explores the effect of finite opening angle of emission, namely that the attenuation is considerably more severe than in Fig. 9 at colatitudes close to the pole.

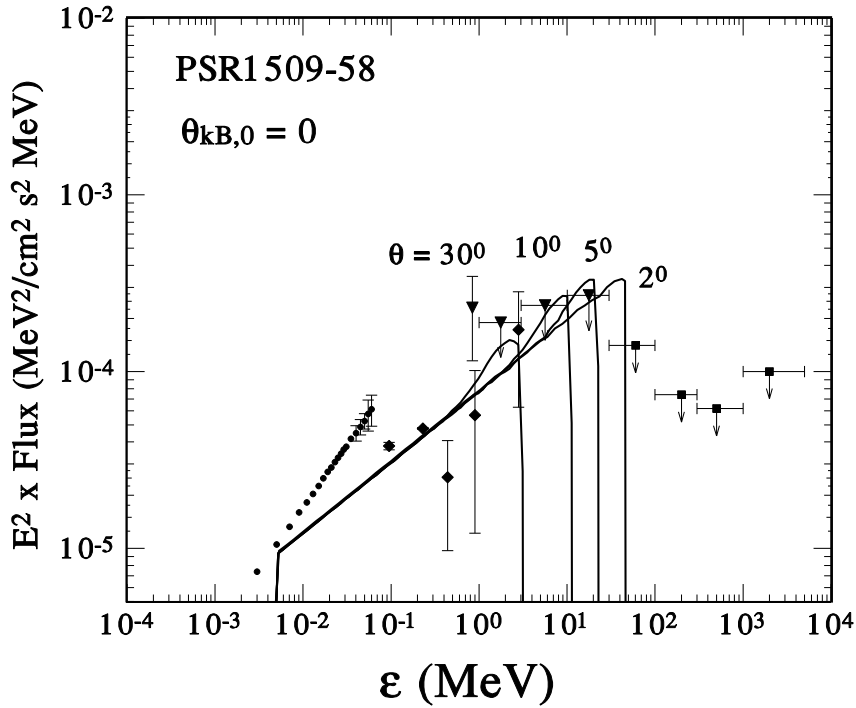


Fig. 11.— Partial photon splitting cascade spectra, obtained by averaging the spectra from Fig. 7 over polarizations and multiplying them by ϵ^2 , compared to the observed spectrum from PSR1509-58. Data points are from GINGA (Kawai, Okayasu, and Sekimoto, 1993): circles, OSSE (Matz et al. 1994): diamonds, COMPTEL (Hermsen et al. 1996): triangles, and EGRET (Nel et al. 1996): squares, and the collective display is an updated version of that in Thompson (1996).

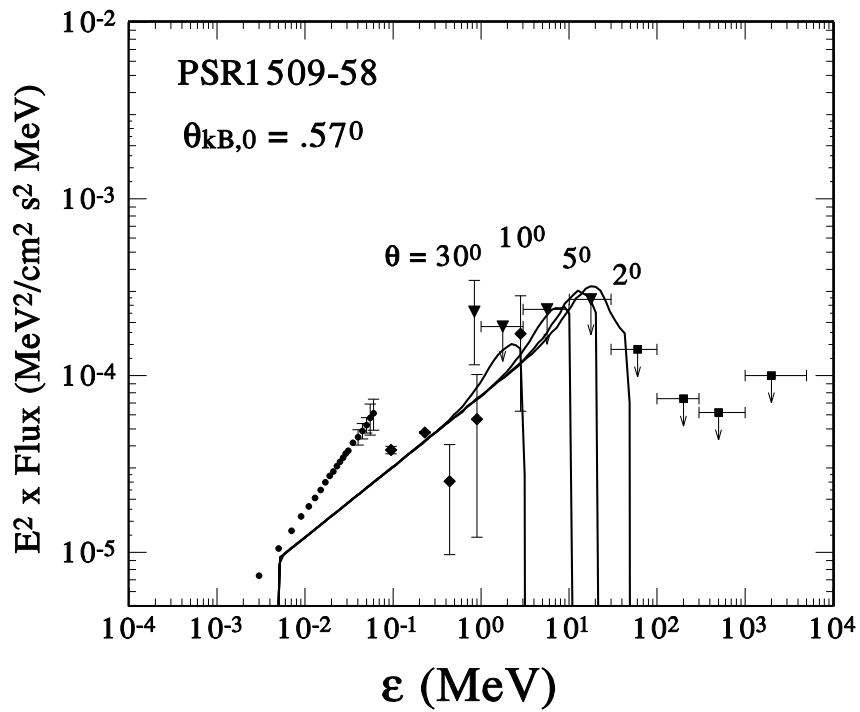


Fig. 12.— Same as Fig. 11, for the model spectra of Fig. 8.

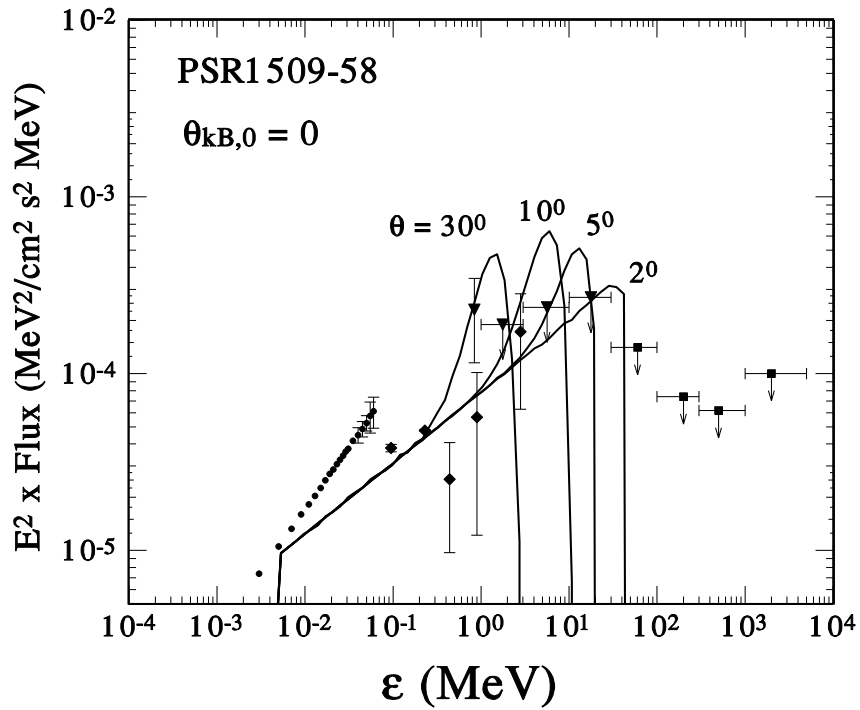


Fig. 13.— The equivalent of Fig. 11 for full splitting cascades, i.e. obtained by averaging the model spectra of Fig. 9 over polarizations and multiplying them by ϵ^2 .

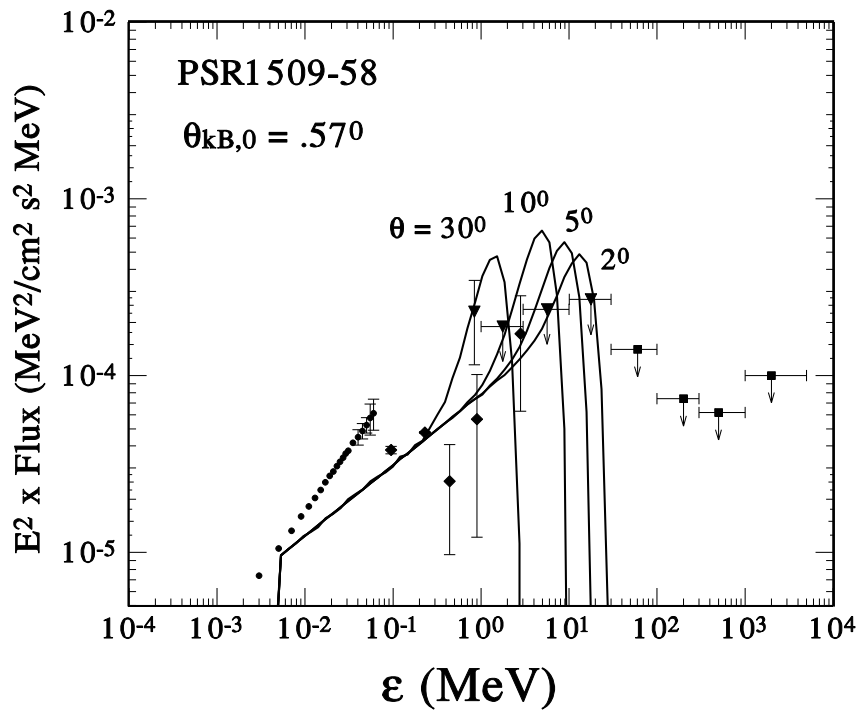


Fig. 14.— Same as Fig. 13, for the model spectra of Fig. 10.